Automated segmentation of tissue structures in optical coherence tomography data

Fernando Gasca
University at Luebeck
Graduate School for Computing in Medicine and Life Sciences
Institute for Robotics and Cognitive Systems
Ratzeburger Alle 160
Lübeck, 23538
Germany
E-mail: gasca@rob.uni-luebeck.de

Lukas Ramrath
University at Luebeck
Institute for Robotics and Cognitive Systems
Ratzeburger Alle 160
Lübeck, 23538
Germany

Gereon Huettmann
University at Luebeck
Institute for Biomedical Optics
Peter-Monnik-Weg 4
Lübeck, 23562
Germany

Achim Schweikard
University at Luebeck
Institute for Robotics and Cognitive Systems
Ratzeburger Alle 160
Lübeck, 23538
Germany

Abstract. Segmentation of optical coherence tomography (OCT) images provides useful information, especially in medical imaging applications. Because OCT images are subject to speckle noise, the identification of structures is complicated. Addressing this issue, two methods for the automated segmentation of arbitrary structures in OCT images are proposed. The methods perform a seeded region growing, applying a model-based analysis of OCT A-scans for the seed's acquisition. The segmentation therefore avoids any user-intervention dependency. The first region-growing algorithm uses an adaptive neighborhood homogeneity criterion based on a model of an OCT intensity course in tissue and a model of speckle noise corruption. It can be applied to an unfiltered OCT image. The second performs region growing on a filtered OCT image applying the local median as a measure for homogeneity in the region. Performance is compared through the quantitative evaluation of artificial data, showing the capabilities of both in terms of structures detected and leakage. The proposed methods were tested on real OCT data in different scenarios and showed promising results for their application in OCT imaging. [DOI: 10.1117/1.3156841]

Keywords: image processing; image segmentation; coherent optical systems; speckle; spatial filtering.

Paper 08223R received Jul. 17, 2008; revised manuscript received Mar. 21, 2009; accepted for publication May 6, 2009; published online Jun. 25, 2009.

1 Introduction

Optical coherence tomography (OCT) is a powerful imaging technique with important applications in several fields. It is, for instance, used in the analysis of biological samples by obtaining high-resolution cross-sectional backscattering profiles.[1] OCT has also been used in several medical applications, mainly ophthalmology, dermatology, and urology.[2] In ophthalmology, OCT scanning of the retina aims at the analysis of the different morphological layers, which contain important structures for the diagnosis of pathological situations. Recent research activities showed that OCT also possesses a strong potential for displaying brain morphology.[3] In this context, OCT imaging aims at providing the surgeon with information at the microscale level, intraoperatively. Applications include the identification of residual tumor tissue or white matter fibers that can be integrated into the navigation environment, such as a microscope, by means of virtual reality.

A crucial role for automated information extraction in medical imaging, such as OCT, usually involves the segmentation of areas of the image for, e.g., quantification of tissue volumes, diagnosis, and localization of pathologies. Image segmentation itself is an ongoing issue in medical image-processing research. Numerous approaches regarding medical image segmentation have evolved in the past and can be classified into eight major categories (see Ref. 4): (*i*) thresholding, (*ii*) region-growing approaches, (*iii*) classifiers, (*iv*) clustering approaches, (*v*) Markov random field models, (*vi*) artificial neural networks, (*vii*) reformable models, and (*viii*) atlas-guided approaches. Their advantages and disadvantages are discussed in Ref. 4. A common approach to segmentation is the above-mentioned region-growing approach (RGA). The goal is to use image characteristics to map individual pixels in an input image to sets of pixels called regions, usually with common properties. Commonly, region growing methods start at the location of a seed and growing is governed by a homogeneity criterion. These criteria can be based on the intensity information and/or edges in the image.[5] General drawbacks of region growing are its user dependency by manual seed placement, sensitivity to changes in the seed's location, leakage, and the difference in the nature of the data to be analyzed.

Segmentation of OCT images has been investigated in limited fields. Primarily in ophthalmology, several approaches have been developed for the segmentation and identification

Address all correspondence to Fernando Gasca, Institute for Robotics and Cognitive Systems, Ratzeburger Alle 160-Lübeck, 23538 Germany; Tel: 49451317 9310; Fax: 494515005202; E-mail: gasca@rob.uni-luebeck.de

1083-3668/2009/14(3)/034046/21/$25.00 © 2009 SPIE

of retinal layers.[6–8] In other fields, such as dermatology, Hori and Yasuno[9] developed a method for automatic segmentation of different structures in the human skin. In Ref. 10, a method for the segmentation of cartilage images from OCT is presented. It is important to note that the former examples focus on images with certain characteristics and do not feature OCT data segmentation in a more general sense.

The segmentation of OCT images generally faces two major problems. First, the intensity course in OCT images results from absorption and scattering of light in tissue. Thus, intensity of a homogeneous area decreases with increasing imaging depth deterministically. This complicates common segmentation approaches, which are usually based on the assumption that intensity variations of homogeneous regions are only due to noise and not inherent to the imaging modality. The second problem is that OCT images are subject to speckle noise, which decreases the image quality and complicates the image analysis.

The latter problem has been targeted by the development of many image-processing methods for enhancement by the means of speckle-noise reduction (see Ref. 11 for an overview). Related techniques originate in the synthetic aperture radar (SAR) community and have been also applied to the field of ultrasonic imaging. To date, commonly applied filters for speckle removal in SAR and ultrasonic images include the Lee,[12] the Frost,[13] and the Kuan filter.[14] The disadvantages of these filters are the output dependency on the size and the shape of the respective filter kernel and the inability to enhance edges that could destroy important information. These drawbacks have led to the development of edge-sensitive or enhancing filters. Some of these filters are based on the solution of a diffusion equation derived from the heat equation and are also known as partial differential equation (PDE)-based anisotropic filters. This approach was first introduced by Perona and Malik and led to the so-called Perona–Malik filter.[15] Generally, these filters encourage smoothing along, while prohibiting smoothing across edges.[15,16] In Ref. 17, the PDE-based formulation is extended to a nonlinear complex diffusion process with a complex valued diffusion coefficient. In recent work on OCT imaging, these two different filtering approaches for OCT images are compared.[18]

Despite the advantage that edge-sensitive filtering enhances the suitability of common RGAs, filtering also alters the image in a way that important information may not enter the segmentation step. On the other hand, if segmentation is performed on unfiltered data, common homogeneity criteria tend to fail because of speckle-noise corruption.

In this work, we propose two approaches to automated seeded region growing for the segmentation of OCT images. Automation of the algorithm is provided by a model-based seed-detection algorithm, which analyzes the intensity profile of an A-scan. Thus, the user dependency is reduced significantly compared to a manual seed selection. In both approaches, the seed detection is followed by a region-growing algorithm. The first approach applies an adaptive neighborhood homogeneity criterion within unfiltered OCT images while the other is based on edge-sensitive filtered images. The ultimate goal of both algorithms is to automatically locate specific structures in OCT images in order to facilitate the usage in diagnosis and/or extraction of morphological information. The information could, for instance, be used for medical navigation, where OCT information is acquired from the probe tip directly and correlated to existing morphological data (e.g., computer tomography data).

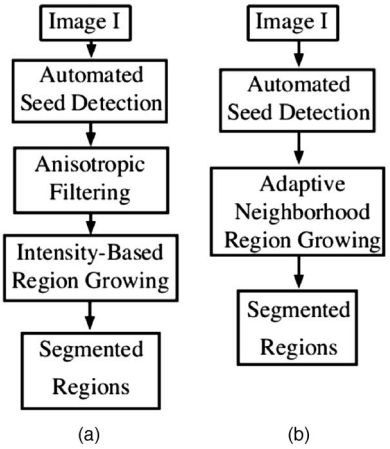

Fig. 1 Flowcharts of proposed region growing approaches: (a) adaptive neighborhood region growing (ARG) and (b) region growing on filtered image (FRG).

The approach is illustrated for the detection and identification of white matter fibers, a valuable application for neurosurgical navigation, where the integration of a real-time imaging modality, such as OCT can provide important information intraoperatively. We also present the application and results for the segmentation of low and highly scattering structures in multiple OCT images, indicating the generality of the proposed approach.

2 Materials and Methods

Both segmentation approaches consist of two steps. The first step, which is common to both algorithms, performs an automated, model-based seed detection. This step forms the basis for the automatic characteristic of the approach. Changes of tissue characteristics are detected by analyzing the intensity profiles that are given by the columns of a B-scan image (A-scans). The detected seeds are used for a region-growing method forming the second step. Two approaches for the region growing featuring different growing criteria are introduced as follows:

1. An adaptive neighborhood region growing (ARG).
2. A filtered-image region growing (FRG) approach based on a edge-sensitive filtered version of the original OCT image.

Although the first approach derives the homogeneity criterion based on an adaptive neighborhood filtering approach and an OCT intensity model, the latter uses statistical measures of the intensity values for the growing process. Figure 1 shows flowcharts for both approaches.

2.1 *OCT and Speckle-Noise Modeling*

OCT is based on the principle of interferometry. The resulting waveform is the sum of the light waves from reference path and sample path. Because being used for imaging purposes in medical applications, analytical models of OCT systems have been developed in order to extract optical properties of tissue to support diagnosis. Different approaches have been pro-

posed. The most advanced models incorporate the multiple-scattering contribution to the OCT signal. Two models are used for extraction of tissue parameters: the radiative transport model[19] and the extended Huygens–Fresnel model.[20] Their analytical expression is divided into three terms, one term representing the single-scattering contribution, another term representing the contribution of multiple-scattering, and the last term denoting the cross relation. See Ref. 20 for a detailed explanation. Turchin et al.[21] derive a theoretical model of the OCT signal for layered media, which integrates small-angle scattering at low depths as well as light diffusion at large depths. The nonlinear model consists of a set of unknown parameters, which are subsequently optimized by a genetic algorithm to fit a measured A-scan profile. Thus, different tissue characteristics can be determined.

In this work, a simplified OCT model based on the single-scattering effect will only be used. Although it does not account for all effects of light propagating through tissue, such as multiple scattering, the simplified model allows linear modeling of the OCT intensity signal. Thus, linear filter theory can be applied and will be done throughout this work. In Ref. 22, the authors propose a model where the measured intensity is proportional to an exponential decay

$$I(z) = I_0 \exp(-2\mu z), \tag{1}$$

where I_0 is the initial intensity and μ denotes the scattering coefficient, and z the scanning depth. In brain imaging, the results in Ref. 23 show that μ differs for various tissue structures (e.g., cortex, external capsule) allowing a clear distinction of white and gray matter. This fact motivates the use of the simplified model for OCT analysis despite its theoretical shortcomings.

In addition to modeling the intensity, speckle noise corrupting OCT images can be modeled statistically. It is usually assumed to be a multiplicative random noise. If f denotes the ideal image and g the speckled image, this assumption can be expressed as

$$g = fu, \tag{2}$$

where u is a signal-independent random variable whose probability density function (PDF) depends on the image type.[12,24] Commonly, the speckle PDF is assumed to follow an exponential distribution described by

$$p_u(x) = \begin{cases} \exp(-x) & \text{if } x \geqslant 0, \\ 0 & \text{otherwise.} \end{cases}$$

In Ref. 24, the speckle mean and standard deviation over a homogeneous and featureless area are derived as

$$\bar{g}_{\text{nom}} = \bar{f}\bar{u} \tag{3}$$

and

$$\sigma_{g_{\text{nom}}} = \bar{f}\sigma_u. \tag{4}$$

This means that the speckle standard deviation is proportional to the mean value of the uncorrupted image in a homogeneous area. The noise level is thus proportional to the local gray level, meaning that a bright area will be more corrupted than a low-intensity area. This important property of speckle noise complicates the general image-processing approaches.

In the following, two contributions to the local intensity at a depth z in an OCT image will be considered:

1. Deterministic contribution. The deterministic part at a depth $z+\Delta z$ evolves from Eq. (1) and can be formulated as

$$I(z+\Delta z) = I_0 \exp(-2\mu z)\exp(-2\mu\Delta z) = I(z)\exp(-2\mu\Delta z) \tag{5}$$

2. Statistical noise contribution. The stochastic noise contribution at depth z will be accounted for according to Eqs. (3) and (4). This means that noise corruption is proportional to the local gray value $I(z)$ at depth z.

2.2 *Automated Seed Detection*

A basic requirement for region growing methods is the specification of seeds, which serve as a starting point for an iterative growing process. A fundamental adept of the proposed method is the automated acquisition of the seeds, derived from an A-scan analysis. An OCT A-scan is a one-dimensional intensity profile over the depth of the scanned sample. The method relies on the simplified model of OCT intensity stated in Eq. (1) and the statistical nature of speckle noise. In a first step, the A-scan course is linearized by applying the natural logarithm operator to Eq. (1)

$$\ln[I(z)] = \ln(I_o) - 2\mu z = \tilde{I}_o + mz. \tag{6}$$

In the computational scenario, the intensity course is discretized. If z_k denotes the depth-related pixel, Eq. (6) can be transformed to

$$\tilde{I}(z_k + 1) = \tilde{I}(z_k) + m'. \tag{7}$$

where m' denotes the pixel-related slope resulting from a scattering coefficient μ.

Automated detection of seeds is exemplary elaborated for white matter detection in OCT images. A good indication of white matter areas in A-scans is based on the high optical contrast of a white matter structure which manifests itself as a sudden increase (spike) in intensity (see Fig. 2). The detection of the spike location can therefore be used as an indicator for white matter areas. Calculating the first derivative of the A-scan intensity course and simple thresholding provides the location of potential white matter regions. A spike at z_k is detected if

$$\tilde{I}(z_k) - \tilde{I}(z_k - 1) > \sigma_1. \tag{8}$$

The corresponding threshold σ_1 is based on gray values per pixel difference. Analyzing the first derivative of the intensity according to Eq. (8) provides a set of white matter–induced peak candidates (see Fig. 2). The signal, however, is also corrupted by speckle noise severely distorting the signal quality. Similar to changes caused by white matter, speckle noise also introduces a spiking characteristic to the intensity signal. This complicates the white matter detection in OCT A-scans, and a robust classification of white matter has to be designed. To differentiate white matter peaks from speckle-noise–induced peaks, two cases can be analyzed. Assume a homogeneous

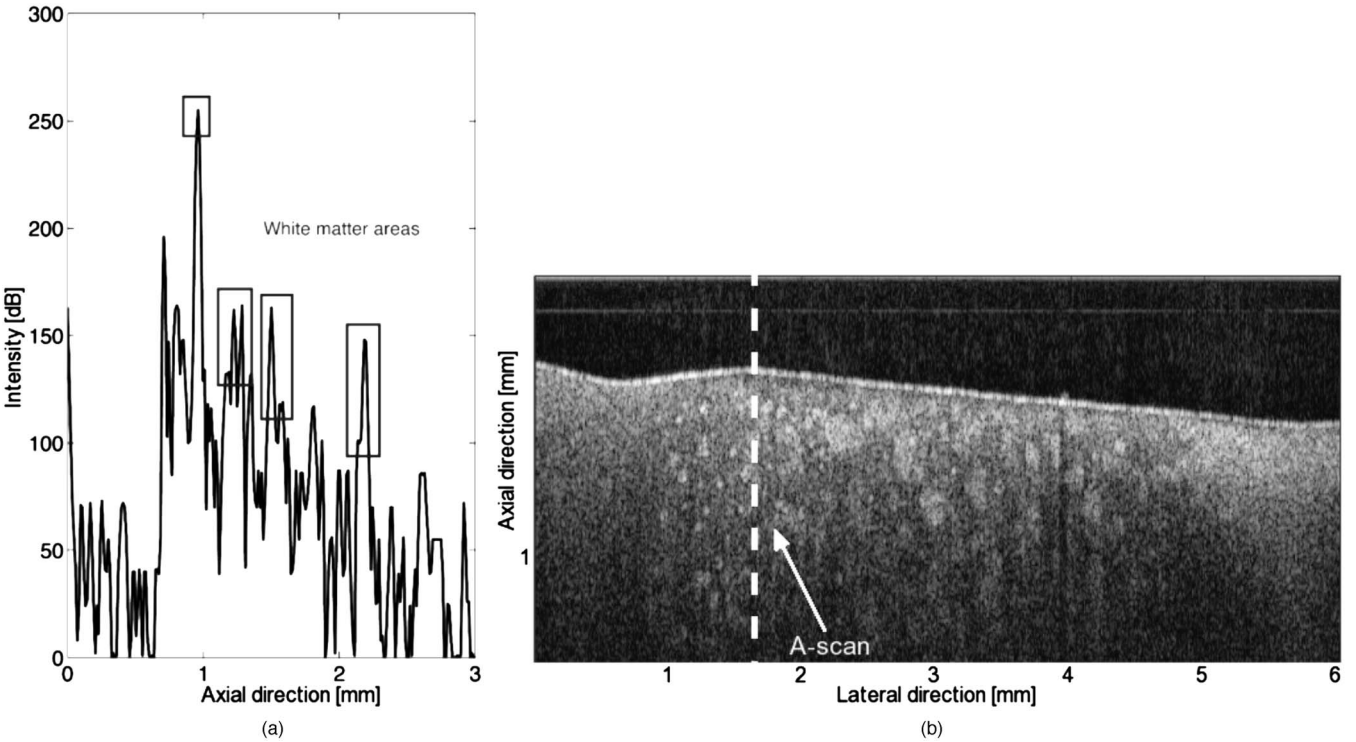

Fig. 2 (a) Sample B-scan of a coronal section of the rat brain and (b) A-scan showing white matter regions.

area with the intensity f. Speckle noise introduces spikes in two ways, as follows:

1. Speckle related spikes results in an intensity increase. Referring to Eq. (2), this corresponds to the case where $u > 1$.
2. Speckle results into a sudden decrease of intensity ($u \ll 1$), which is then followed by a sudden increase to the ideal intensity f, which would subsequently be detected as a peak candidate.

The set of white matter–induced peak candidates is now refined by analyzing the following two criteria:

1. Assume an intensity spike because of $u > 1$ at the location z_k is introduced by speckle noise. Because speckle noise features random characteristics, the intensity at pixels following the spike most probably drop again. White matter areas, however, will show a slow increase with a characteristic slope [see Eq. (7)]. Therefore, white matter can be classified if the ratio

$$\frac{\tilde{I}(z_k+n)}{\tilde{I}(z_k+n-1)} > \sigma_2 \quad \text{for} \quad n=[1 \ldots l_T]. \tag{9}$$

   Here, σ_2 denotes a slope-related threshold and l_T the length of the white matter tail.
2. For speckle related spikes according to the second scenario $u \ll 1$, an additional measure is introduced. It relates the intensity at the detected spike location z_k to the mean of intensities previous to the spike location. A white matter–related spike is detected if

$$\frac{\tilde{I}(z_k)}{[\Sigma_{n=1}^{N}\tilde{I}(z_k-n)]/N} > \sigma_3. \tag{10}$$

   Here, N denotes the number of pixel locations previous to the spike, which will be taken into account.

White matter detection is now done by analyzing the A-scan and its derivate. A set of peak candidate is found according to the criterion given in Eq. (8). Subsequently, criteria Eqs. (9) and (10) are used to find the set of true white matter–induced peaks. Figure 3 shows results for an exemplary A-scan.

After having identified seed candidates in the OCT A-scan, a third robustness measure, called a low-consistency check, is introduced. The location of detected seeds is compared to the location of detected seeds in the neighboring A-scans. Therefore, a 5×5 window with its center being the current seed is analyzed. If this window contains more than four additional seeds, then the current seed is approved.

Performance of the proposed seed detection scheme is strongly dependent on the threshold parameters σ_1, σ_2, and σ_3. Heuristics for the choice of the thresholds and the overall performance evaluation is based on an extensive analysis of simulated B-scans (see Sec. 3.2). The proposed seed-detection algorithm is now summarized in the following definition.

Definition 1. *Let I denote an image. Then,*

$$S = \text{seedDetection}(I, \sigma_1, \sigma_2, \sigma_3) \tag{11}$$

is defined as the set of seed pixels provided by the A-scan intensity course based white matter detection.

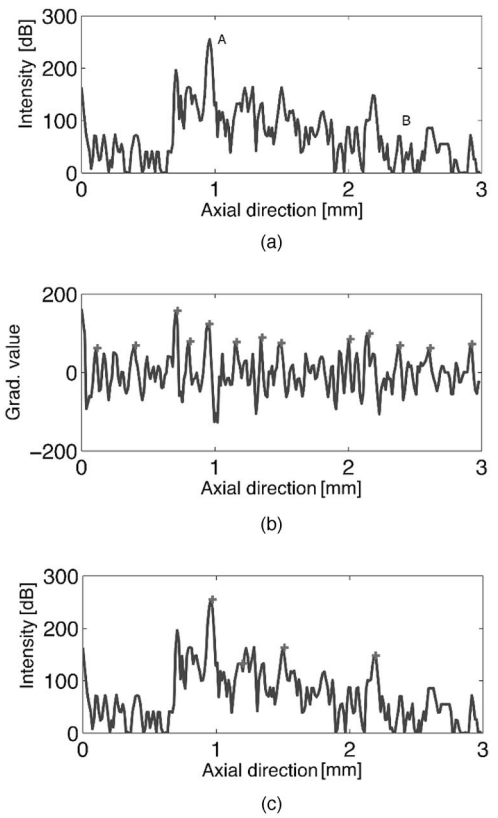

Fig. 3 Seed detection in OCT image of a coronal section of the rat brain with embedded white fibers: (a) Original A-scan, (b) first derivative of the A-scan and proposed peaks indicated by gray crosses, and (c) original A-scan with classified white matter peaks indicated by gray crosses.

2.3 *Adaptive Neighborhood Region Growing (ARG)*

Common region growing approaches tend to fail in OCT images because of the exponential decay according to Eq. (1) and the speckle-noise corruption. This is because the OCT signal properties and the dependency of the noise on the local intensity is not reflected by the homogeneity criteria used in those methods. Resulting from research in the image-filtering community, adaptive filters have been developed that estimate the speckle standard deviation σ_u based on the local mean.[24] The approach has proven to be well suited for filtering of SAR images. For OCT images, however, this approach is not optimal as the intensity level follows a deterministic behavior as shown in Eq. (1). To perform region growing based on adaptive neighborhood filtering, the approach will be extended by incorporating the OCT intensity model into the homogeneity criterion. The approach is based on the following ideas:

1. The homogeneity or growing criterion for OCT images will be affected by two parts: a deterministic part incorporating the modeled behavior as in Eq. (1) and a stochastic part based on the local average and standard deviation.

2. The speckle-noise standard deviation $\sigma_{g_{\text{hom}}}$ is not known *a priori* and will be estimated within a local neighborhood according to Eq. (4) (as proposed in Ref. 24).

In the following, an adaptive homogeneity criterion based on the evaluation of local statistics and the deterministic model in Eq. (1) will be developed. The criterion uses the median to estimate the central tendency locally, as in Ref. 25. The median is robust in terms of outliers, which in this case, suits the purpose due to the presence of speckle noise. Additionally, it is simple to implement. To introduce the approach the following definitions are made.

Definition 2. *Let s denote a pixel of a speckle noise corrupted image g. Then $\Gamma_n(s)$ denotes the $n\times n$ neighborhood of s and $\Gamma_{n,y}(s)$ denotes the $n\times 1$ rowwise neighborhood in the row y (neighboring pixels in the same row).*

Definition 3. *Let s denote a pixel of a speckle noise corrupted image g and $g(s)$ the gray value at pixel s. Let q be a pixel and element of $\Gamma_n(s)$. The confidence interval $[T_1,T_2]$ for q determines the range of valid $g(q)$ values for it to become part of the current region and is given by*

$$T_1(q) = g_{\text{med}}(q) - c_1\frac{u}{\bar{u}}g_{\text{med}}(q),$$

$$T_2(q) = g_{\text{med}}(q) + c_2\frac{u}{\bar{u}}g_{\text{med}}(q). \tag{12}$$

where c_1 and c_2 are confidence interval shift parameters and

$$g_{\text{med}}(q) = \begin{cases} \text{median}[\Gamma_{n,z}(s)]\exp(-2\mu\Delta y) & \text{if } q_z > s_z, \\ \text{median}[\Gamma_{n,y}(s)] & \text{if } q_z = s_z, \\ \text{median}[\Gamma_{n,y}(s)]\exp(2\mu\Delta z) & \text{if } q_z < s_z \end{cases}$$

where s_z and q_z denote the z-coordinate of the pixel, which corresponds to the imaging depth and Δz their depth difference. The adaptive region growing homogeneity criterion is then defined as

$$\text{homARG}(q,s) = \begin{cases} \text{true} & \text{if } g(q) \in [T_1,T_2] \\ \text{false} & \text{otherwise.} \end{cases}$$

For the definition of $g_{\text{med}}(q)$, the OCT intensity exponential decay model is considered. Where, if an evaluated pixel q is located at a lower depth than the seed s, then the estimation will consider a positive exponential; whereas if pixel q is located at at higher depth that s then the estimation will consider the negative exponential decay. If pixels s and q have the same depth, then the local statistical situation is considered through the median. On the basis of the mentioned observations and definitions above, the following steps are taken for the ARG:

1. Obtain an initial seed set S by performing the seed detection.
2. Estimate the local average $\bar{g}_{\text{hom}}$ as the row-wise median $\Gamma_{n,y}(s)$ within the row of the seed pixel s.
3. For every pixel q in a 3×3 neighborhood of a seed pixel s, calculate the confidence interval according to Eq. (12) and evaluate the membership to the region according to the homogeneity criterion.
4. If membership is given, meaning the homogeneity criterion is fulfilled, include the neighbor pixel q into the seed set S and the set of detected white matter R.
5. Stop the region growing if the seed set S is empty.

The main advantages of the approach are the adaptivity of the homogeneity criterion, the integration of the deterministic in-

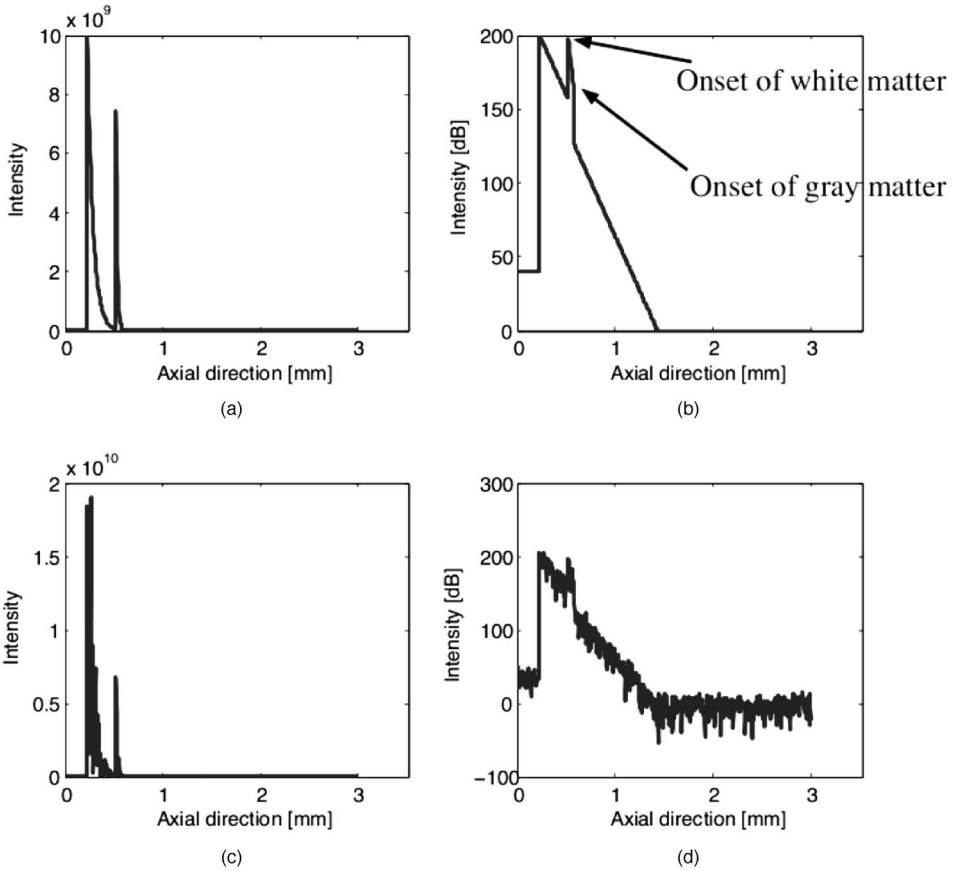

Fig. 4 Simulated OCT A-scan with one embedded white matter area: (a) Uncorrupted A-scan data, (b) linearized uncorrupted A-scan with arrows showing the embedded white matter region, (c) corrupted A-scan data, and (d) linearized corrupted A-scan data.

tensity decay, and the integration of speckle-noise corruption into the homogeneity criterion. Thus, the region growing is able to work on an unfiltered OCT image.

2.4 *FRG*

As stated in Sec. 1, numerous noise-removal techniques have been developed for the reduction of speckle-noise corruption. Filters that do not support edge preservation are generally not suitable for RGA. Edge-sensitive or enhancing filters, however, try to smooth along edges and not across them, thus being good candidate filters for subsequent region growing approaches. The review of recent OCT-related literature[18] shows that the Perona–Malik and the complex diffusion filter are suitable approaches for OCT image filtering. Although the Perona–Malik serves primarily as a edge-preserving denoising process,[15] the complex diffusion filter performs even better denoising image, also avoiding staircasing,[17] which can be an additional source of artifacts. For the rest of this work, the following definitions will be used:

Definition 4. *Let I denote a gray-valued image. Then*,

$$\hat{g} = \mathrm{pmFilter}(g, N, K) \tag{13}$$

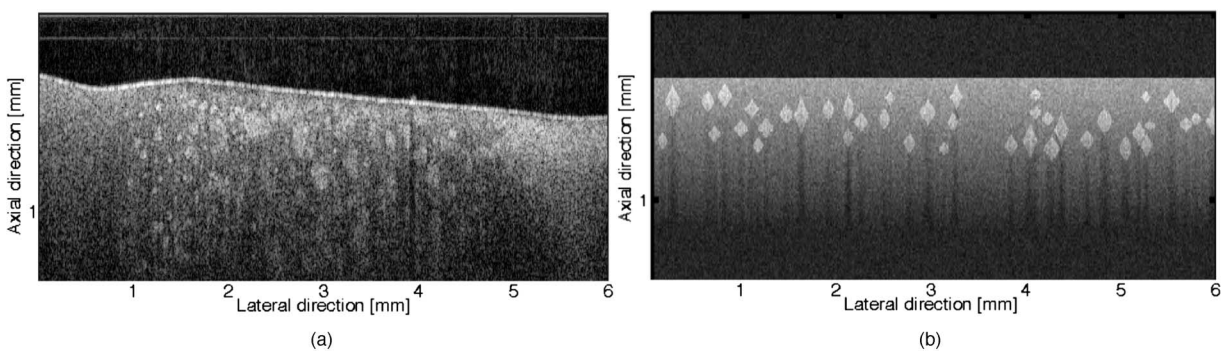

Fig. 5 Simulation of OCT B-scan images of a coronal section of the rat brain with embedded white fibers: (a) Real white fibers embedded into gray brain matter and (b) simulated white fibers embedded into gray brain matter.

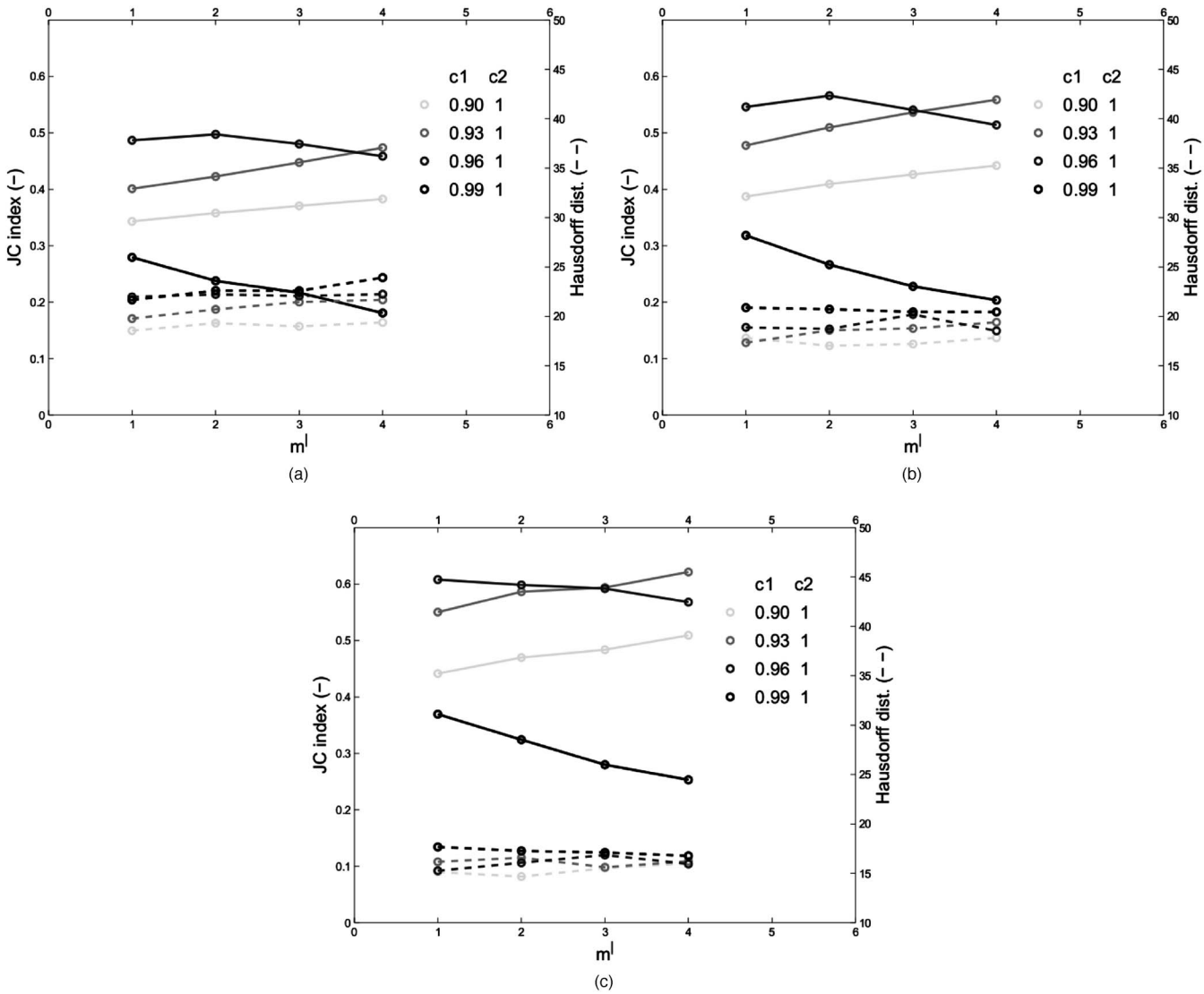

Fig. 6 JC index and HD for different parameters m' and c_1 for the ARG approach with: (a) PCR=20, (b) PCR=25, and (c) PCR=30. The best compromise for the two performance measures is in the interval of $c_1=0.93\ldots0.97$.

is defined as the edge-sensitive filtered version of g according to Ref. 15.

In this formulation, N denotes the number of iterations and K denotes the edge threshold parameter. In Ref. 17, the concept is extended to a complex diffusion process.

Definition 5. *Let I denote a gray-valued image. Then,*

$$\hat{g} = \mathrm{cdFilter}(g,N,K) \tag{14}$$

is defined as the complex diffusion filtered version of g according to Ref. 17.

Filtering according to both approaches incorporates the following features:

1. region smoothing
2. edge enhancing

Region growing for the filtered version of the image follows the same guidelines as the ARG approach except that the homogeneity criterion is chosen differently. This is because the intensity distribution in the image is altered and the effect of speckle noise is reduced through the filtering process. In fact, the criterion can now be selected as a simple, intensity-based criterion employing the median operator.

Definition 6. *Let s denote a pixel of a speckle noise corrupted image g and $\hat{g}$ the filtered version. Let $\hat{g}(s)$ denote the gray value at pixel s. Let $q \in \Gamma_n(s)$. Then, the confidence interval $[T_1,T_2]$ at q is given by*

$$T_1(q) = c_1 \cdot \mathrm{median}[\hat{\Gamma}_n(s)],$$

$$T_2(q) = c_2 \cdot \mathrm{median}[\hat{\Gamma}_n(s)], \tag{15}$$

where c_1 and c_2 are confidence interval shift parameters. The filtered region growing homogeneity criterion is then defined as

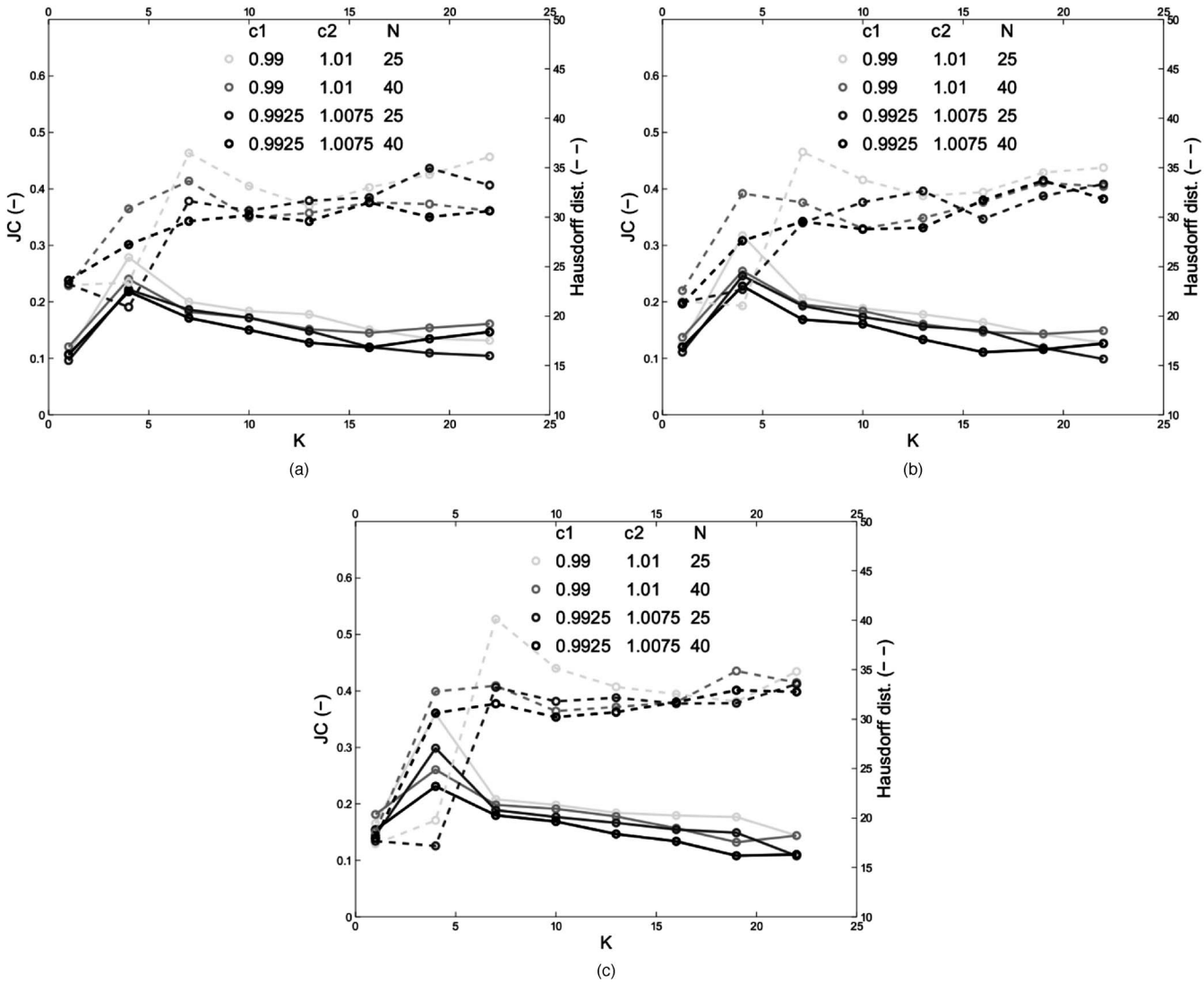

Fig. 7 JC index and HD for different parameters N, K, and c_1 for the PM-FRG approach with (a) PCR=20, (b) PCR=25, (c) PCR=30. The best compromise for the two performance measures is located at $K \approx 4$ with $c_1=0.99$ and $c_2=1.01$.

$$\text{homFRG}(q,s) = \begin{cases} \text{true} & \text{if } \hat{g}(q) \in [T_1, T_2] \\ \text{false} & \text{otherwise.} \end{cases}$$

3 Results

3.1 *Simulated B-Scan*

Performance evaluation of both segmentation approaches is achieved through the simulation of white matter fibers in artificial B-Scans. Hereby, an artificial B-scan is composed of a fixed number of artificial A-scans, which are generated according to the intensity model shown in Eq. (1). Two tissue structures, namely, white and gray brain matter, are incorporated by using different scattering coefficients μ_{WM} and μ_{GM} respectively. Generally, the basic decay with increasing depth is assumed to be governed by gray-matter scattering. At random depth locations, white matter areas are introduced by two means, as follows:

1. intensity increase
2. change of scattering coefficient $\mu_{\text{GM}} \rightarrow \mu_{\text{WM}}$

The intensity increase at a white matter location is given by the peak contrast ratio (PCR), which is defined next.

Definition 7. *Let g denote a gray-valued image. Let* $p_{q_{z-1}}$ *and* p_{q_z} *denote neighboring pixels in one column and let* $p_{q_{z-1}}$ *be an element of a gray matter area and* p_{q_z} *be an element of white matter area. Then*,

$$\text{PCR} = \frac{g(p_{q_z})}{g(p_{q_{z-1}})} \tag{16}$$

is defined as the PCR of white and gray matter areas.

The size of the white matter region can also be chosen randomly. After generating the ideal intensity course, signals were contaminated with artificial multiplicative noise under the model of

Table 1 Averaged seed-detection performance for varying PCR for $n=100$ of simulated B-scans.

PCR	% of detected white matter structures	% of false positive detected seeds
20	0.91	0.07
25	0.95	0.04
30	0.98	0.02
40	0.98	0.007
50	0.98	0.001

$$g = fu,$$

where $u(n)$ is a stationary noise process which has mean 1 and variance σ_u^2.

Figure 4 visualizes the concept. To each image, a fixed number of fibers was added. Size and location of the fibers were randomly chosen. This way, the simulation reproduced an approximate behavior of the presence of white matter fibers in brain tissue. In Fig. 5, the artificial B-scan and the embedded fibers are shown.

3.2 *Seed Detection*

The seed detection algorithm presented in Sec. 2.2 was evaluated in order to find the optimal set of parameters σ_1, σ_2, and σ_3 for different PCR of structures in the image. Therefore, artificial B-scans as described in Sec. 3.1 were created and a measure for the seed-detection performance was evaluated for different parameters σ_1, σ_2, and σ_3. Performance evaluation is based on the following two measures:

1. Percentage of detected white matter structures. The percentage of detected white matter structures can be understood as the sensitivity of the seed-detection process. It indicates how many structures (not pixels) are identified by at least one seed and will therefore enter the region-growing process.

2. Number of false positive seeds. The seed detection related false positive ratio gives the percentage of false positive seeds against the total number of detected seeds.

Evaluation of the parameters was performed on the averaged results of $n=100$ artificial B-scans. Results were obtanied in terms of a modified receiver operating curve (ROC). The modified ROC plots the percentage of detected white matter structures (equivalent to the sensitivity) against the false positive rate of the seed detection. The following effects of the parameter choice on the seed-detection performance can be deduced from the ROC analysis:

1. The choice of $\sigma_2=1.25$ outperforms other parameter settings in terms of the false positive and the percentage of detected structures.

2. The choice of $\sigma_1=40$ yields the best results. This parameter choice is also supported for other PCR scenarios (PCR=20 and PCR=30).

3. The choice of σ_3 can be seen as a trade-off between the percentage of detected structure and the false-positive rate. A choice of $\sigma_3=0.5$ yields a better sensitivity for white matter structure detection but a higher false-positive rate. The higher σ_3, the lower the sensitivity and the false positive detected seeds. This leads to a choice of $\sigma_3=[0.5\ldots0.7]$.

Based on the findings, the following parameters are chosen to obtain numerical results of the seed detection: $\sigma_1=40$, $\sigma_2=1.25$, and $\sigma_3=0.5$. Table 1 provides the numerical results of the seed detection performance. All simulations were considering parameter values $N=4$ and $l_T=3$. The choice of these parameters takes into account the capacity to detect very small regions. If these parameters were set to higher values, then they would reach a point in which they could mistake two adjacent regions.

3.3 *Segmentation Performance Measures*

The performance measures for both RGAs (ARG, FRG) were chosen as follows:

1. The Jaccard (JC) index.[26] It is given as

$$\mathrm{JC} := \frac{|X \cap Y|}{|X \cup Y|}, \tag{17}$$

where X is a set of segmented pixels in the image to be evaluated and Y is the set of segmented pixels in the reference image (desired segmentation). The operator $\|$ stands for the number of elements. This similarity measure is equal to 1 if X and Y are the same region and zero if they are disjoint regions.

2. The Hausdorff distance (HD).[27] The HD defines the largest difference between two contours and is a well-accepted measure for leakage.

Table 2 Averaged results for region growing approaches for $n=100$ simulated B-scans. Shown are the mean, maximal, and minimal JC index, HD and time consumption for a contrast ratio of PCR=20 of the simulated B-scans. Parameters of the respective filters were chosen such that the mean JC index is in the same range.

	JC index			HD			Time (s)		
	Mean	Maximum	Minimum	Mean	Maximum	Minimum	Mean	Maximum	Minimum
ARG	0.4887	0.5442	0.4168	19.05	31.95	13.60	1.57	2.15	0.93
PM-FRG	0.2869	0.3486	0.2273	22.30	36.72	12.73	0.53	0.75	0.41
CD-FRG	0.3025	0.4549	0.1925	25.91	47.38	13.60	0.89	1.15	0.75

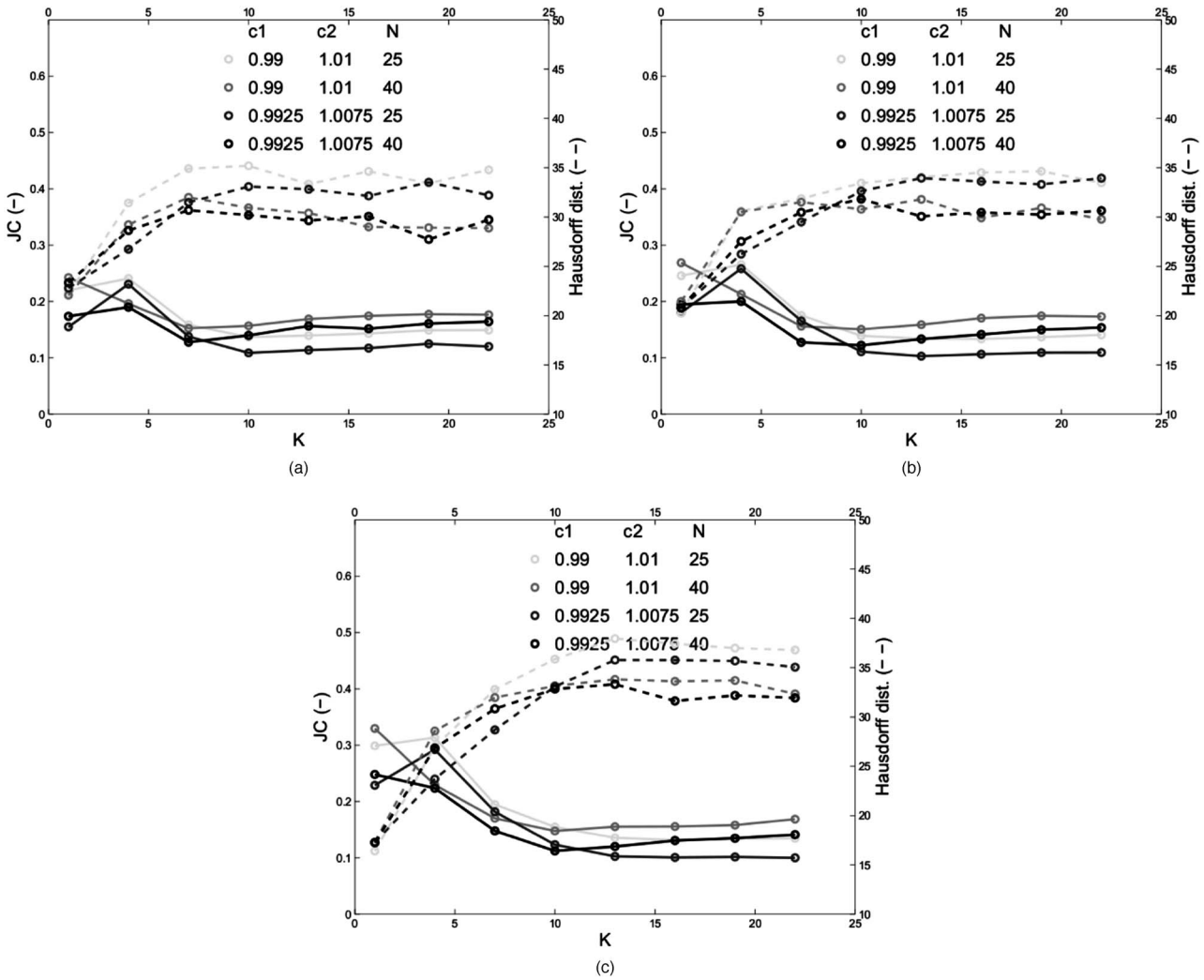

Fig. 8 JC index and HD for different parameters N, K, c_1 for the CD-FRG approach with: (a) PCR=20 and (b) PCR=25, (c) PCR=30. The best compromise for the two performance measures is located at $K \approx 4$ with $c_1=0.99$ and $c_2=1.01$.

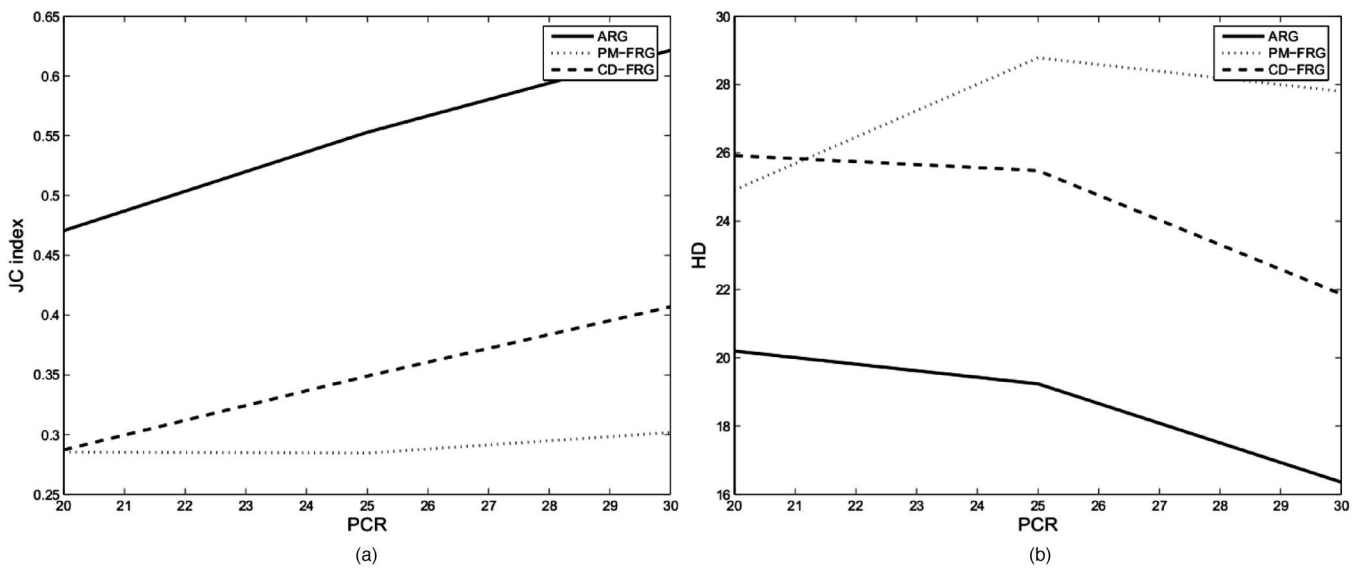

Fig. 9 ARG and FRG performance in terms of averaged (a) JC index and (b) HD of white matter segmentation for different PCR in simulated OCT B-scans for the ARG and FRG.

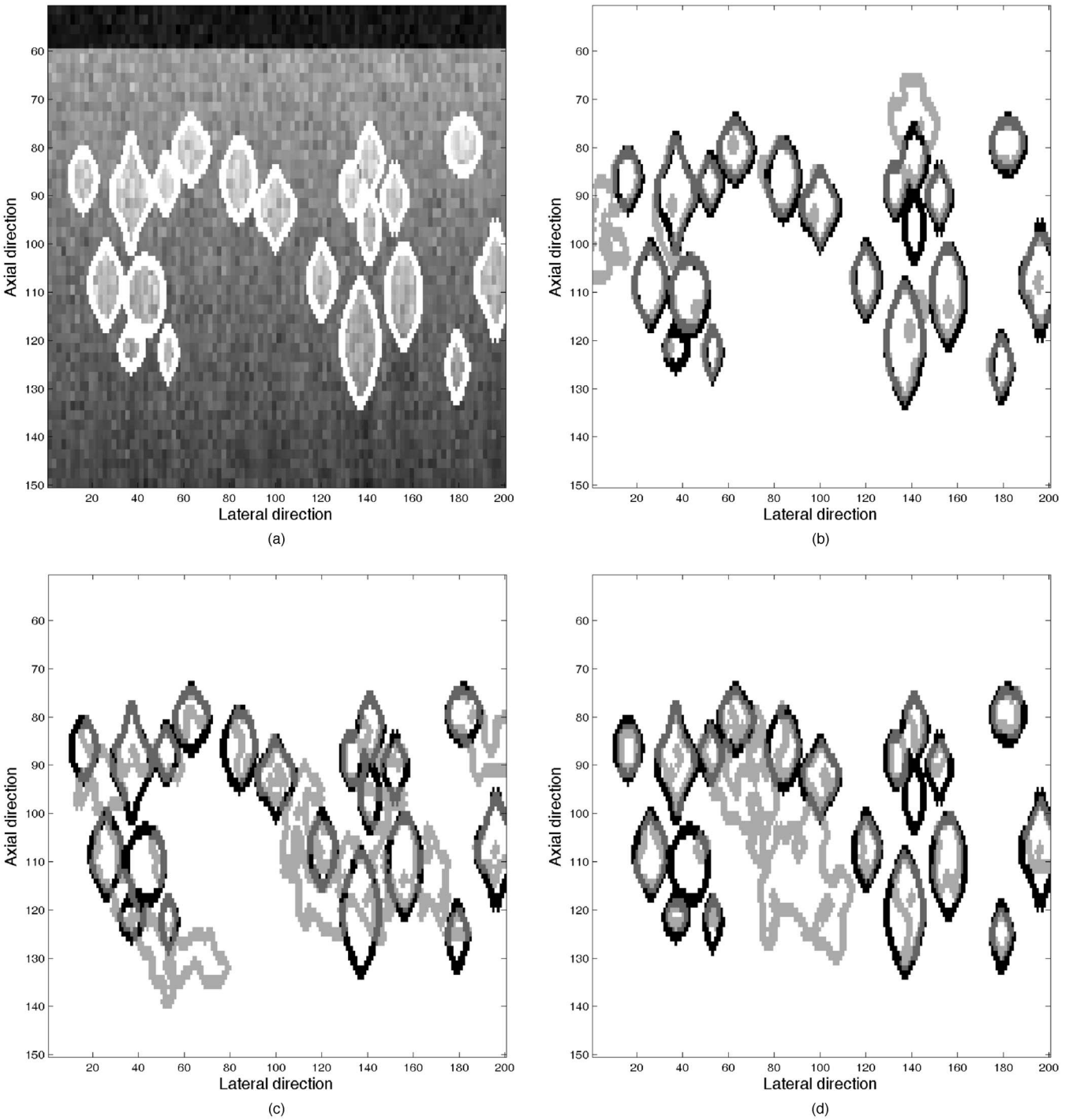

Fig. 10 Comparison of three region growing approaches for segmentation of a white matter fibers in simulated B-scans of brain matter (PCR =20): (a) Exemplary simulated OCT B-scan showing white matter structures with manual segmentation results, (b)ARG, (c) PM-FRG, and (d) CD-FRG. For each evaluated method, the segmentation map shows the reference (manual segmentation) in black and the methods results in gray. In the places where they overlap, darker gray is noted.

3. Time. All results were obtained on a PC with 2.4-GHz processing unit and 2 GB of RAM.

3.4 *Simulation Results*

Automated white matter detection was evaluated on $n=100$ test images with 400×512 pixels. Twenty white matter regions with random location and random size were simulated in the test images. The images were subsequently corrupted by speckle noise following an exponential PDF, as shown in Eq. (3). The standard deviation of the noise was chosen to be $\sigma_u=1$. Different peak contrast ratios were analyzed.

Segmentation results of both, ARG and FRG approaches with edge-sensitive filtering, are dependent on certain parameters. To derive an adequate choice of parameters, different

Table 3 Real OCT imaging scenarios.

Scenario	Region of interest	Figure	Imaging source
wm1	White matter fibers in coronal rat brain section	11	Swept Source Microscope System (Thorlabs, Inc., Newton USA)
wm2	White matter fibers in coronal rat brain section	12	Spectral radar OCT imaging system (Thorlabs HL GmbH, Luebeck, Germany) center wavelength at 930 nm
Onion	Onion cell walls	13	Spectral radar OCT imaging system (Thorlabs HL GmbH, Luebeck, Germany) center wavelength of 830 nm
Urothel	Vessels embedded into urothel	14	Time domain OCT imaging system (4optics GmbH, Heidelberg, Germany) center wavelength of 1310 nm
Intestine	Vessels embedded into intestine wall	15	Spectral radar OCT imaging system (Thorlabs HL GmbH, Luebeck, Germany) center wavelength of 830 nm
Egg	Vessel embedded inner skin of egg	16	Spectral radar OCT imaging system (Thorlabs HL GmbH, Luebeck, Germany) center wavelength of 940 nm

parameter settings were analyzed with respect to the JC index and the HD.

3.4.1 *ARG parameters*

In the ARG scenario, the parameters to be varied are the scattering coefficient m' and the confidence interval shift parameters c_1 and c_2. In Fig. 6, the JC index and HD are shown for different PCRs and parameter sets. The following observations can be made: generally, the higher the JC index is, the higher the HD is, which requires the user to find a trade-off between segmentation quality and leakage. For all PCR scenarios, the following effect of the confidence shift parameter can be observed: a low shift parameter (e.g., $c_1=0.90$) leads to a small JC index and a low HD. A high shift parameter (e.g., $c_1=0.99$) also leads to a small JC index but a higher HD. The optimum value of the shift parameter is therefore in the range $c_1=0.93\ldots0.97$.

Observing the simulated segmented images and the changes induced by different values of shift paramenter c_1, it was noted that the ratio of correctly identified white matter pixels over the number of existing white matter pixels, as well as the ratio of falsely identified white matter pixels over the number of existing white matter pixels, decreased as the c_1 parameter increased. This indicates that a lower interval shift parameter imposes less constraints on the growing process and therefore identifies more structures of interest but results in a higher false positive rate. For a high interval shift parameter $c_1=0.99$, the ARG identifies only a small subpart of the white matter structures which leads to the low JC index. Interestingly, the HD is still high. This is due to the fact that the largest difference between the two contours is not due to leakage but due to the difference of the true contour to the much stricter segmented version. Extensive simulations have shown that the parameter c_2 does not influence the results in the white matter–detection scenario significantly. This is because seeds are already located in high-intensity areas. Leakage mostly occurs if the lower bound of the confidence interval is chosen to be low, which leads to the integration of neighboring gray matter.

The scattering coefficient m' is actually a characteristic property of distinct tissue structures. The exact numerical value, however, is not necessarily known before the segmentation. Therefore, the choice of different m' has also been examined. According to Fig. 6, an increasing scattering coefficient m', which also influences the growing process [see Eq. (12)], leads to an increase of the JC index and the HD. A good trade-off between JC index and HD is therefore achieved if $c_1=0.93$, $c_2=1$, and $m'=4$.

3.4.2 *FRG*

For the FRG parameters, the two scenarios PM-FRG and CD-FRG have been evaluated. In both cases, the following parameters can be varied: the edge threshold parameter K, the number of iterations N, and, as for the ARG case, the choice of confidence interval shift parameters c_1 and c_2 [see Eq. (15)]. The results for the PM-FRG scenario are shown in Fig. 7 for different PCRs. The following observations can be made: with increasing number of iterations, the JC index increases and the HD decreases. For decreasing values of the confidence interval shift parameter c_1, the same observation holds. With increasing the edge threshold parameter K, the HD increases almost linearily while the JC index features a local optimum at threshold parameters $K=4\ldots10$. For $K=11\ldots20$, the JC index decreases. The performance of the CD-FRG (see Fig. 8) almost features the same characteristics although at PCR=20, the local optimum of the JC index is not distinct. A good trade-off between JC index and HD is therefore achieved for low values of K (e.g., $K=3\ldots5$). The number of iterations and the confidence interval parameter c_1 should be chosen according the desired leakage performance.

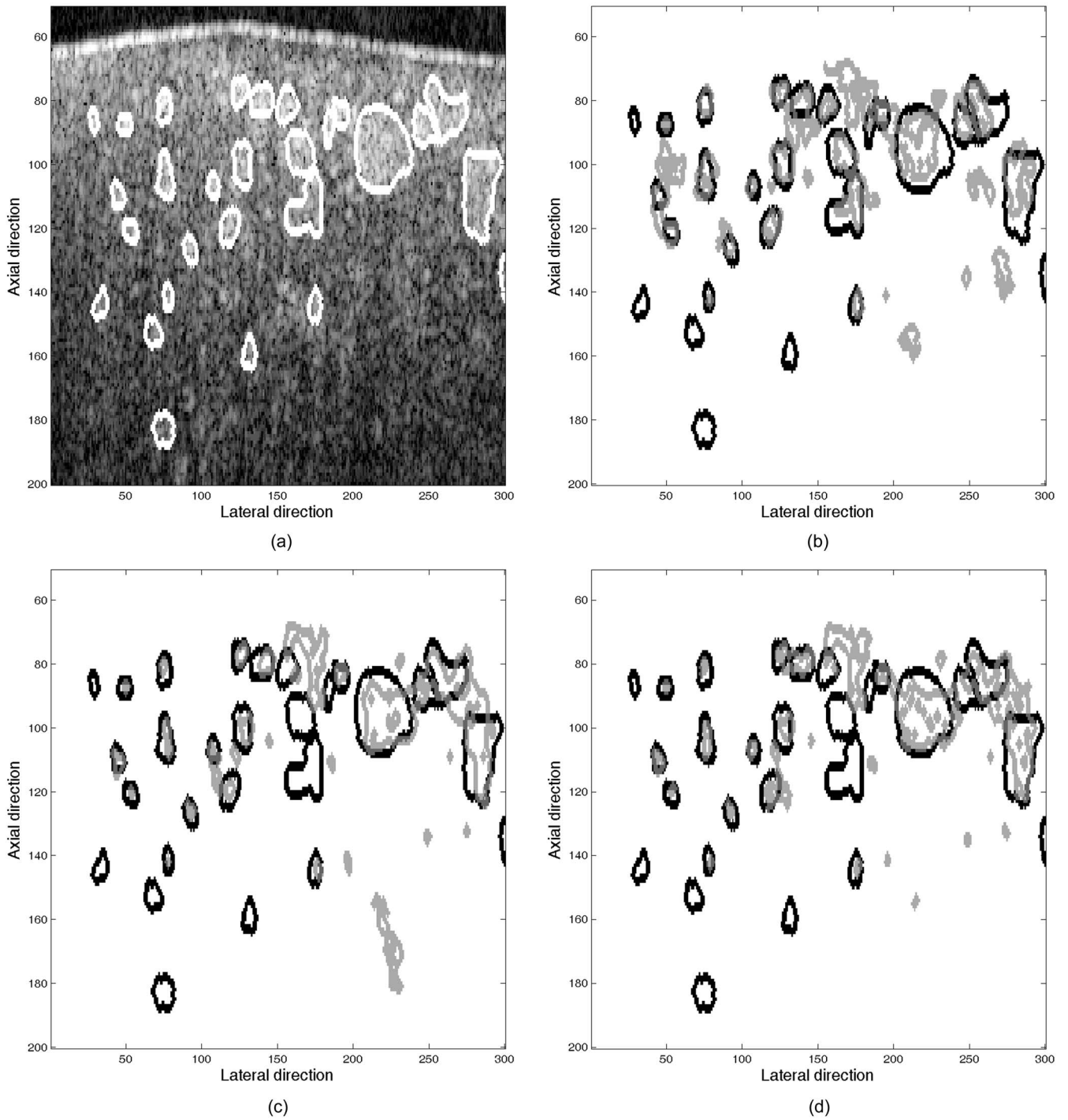

Fig. 11 Scenario wm1: Comparison of three region growing approaches for segmentation of a white matter fibers brain tissue: (a) OCT B-scan showing brain matter with embedded white matter fibers and manual segmentation. (b)ARG, (c) PM-FRG, and (d) CD-FRG. For each evaluated method the segmentation map shows the reference (manual segmentation) in black and the methods results in gray.

The major difference between the ARG and the FRG approaches can already be observed. For all parameter settings, the FRG approaches perform worse in terms of JC index and HD distance. For an equal HD performance, the JC index of the FRG approaches is much lower than for the ARG approach and there is no parameter choice for the FRG approaches, which would provide the same performance. For further comparison of both, ARG and FRG, the parameters N, K, and c_1 were chosen as $N=40$, $K=4$, $c_1=0.99$, and $c_2=1.01$.

In order to further elaborate the different characteristics of ARG and FRG approaches, Table 2 shows averaged quantitative results for $n=100$ simulated B-scans at a PCR of 20. Figure 9 visualizes the performance for different contrast ratios based on an evaluation of $n=100$ simulated B-scans. Fig-

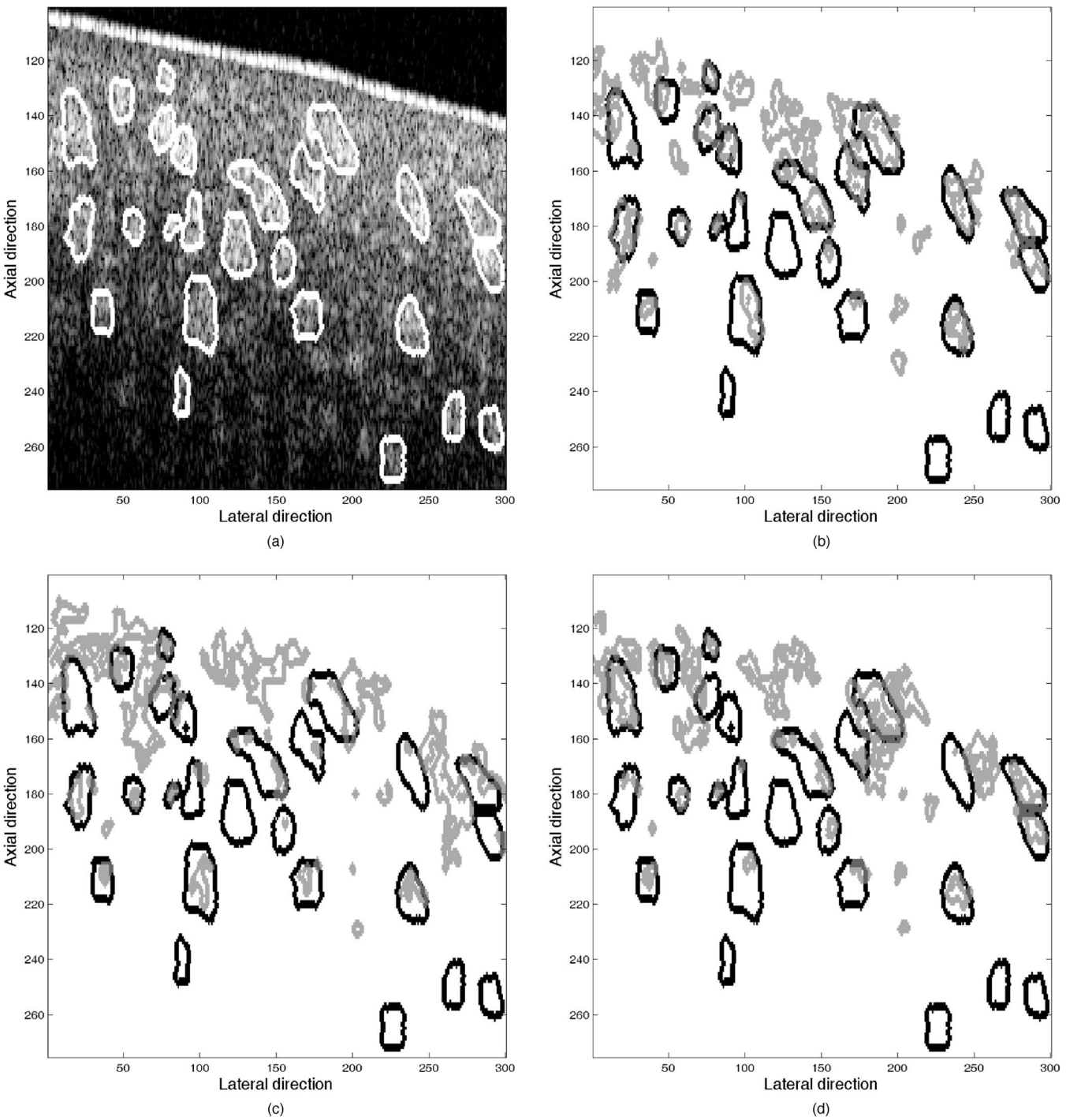

Fig. 12 Scenario wm2: Comparison of three region growing approaches for segmentation of a white matter fibers in brain tissue: (a) OCT B-scan showing brain matter with embedded white matter fibers and manual segmentation, (b) ARG, (c) PM-FRG, and (d) CD-FRG. For each evaluated method, the segmentation map shows the reference (manual segmentation) in black and the methods results in gray.

ure 10 shows an exemplary segmentation result for a PCR of 20. In all cases, the parameters were chosen as discussed above.

3.5 *Real Results*

To show the performance of the three approaches for the segmentation of real OCT images of biological tissue, two image types with different segmentation criteria were tested.

3.5.1 *Segmentation of highly scattering structures such as white matter*

Possible applications of white matter segmentation include the integration of OCT into neurosurgical settings (e.g., into an operating microscope). This would provide the surgeon with detailed tissue information during the operation, which would benefit especially within delicate surgeries. Three test images were acquired from the brain of a freshly decapitated

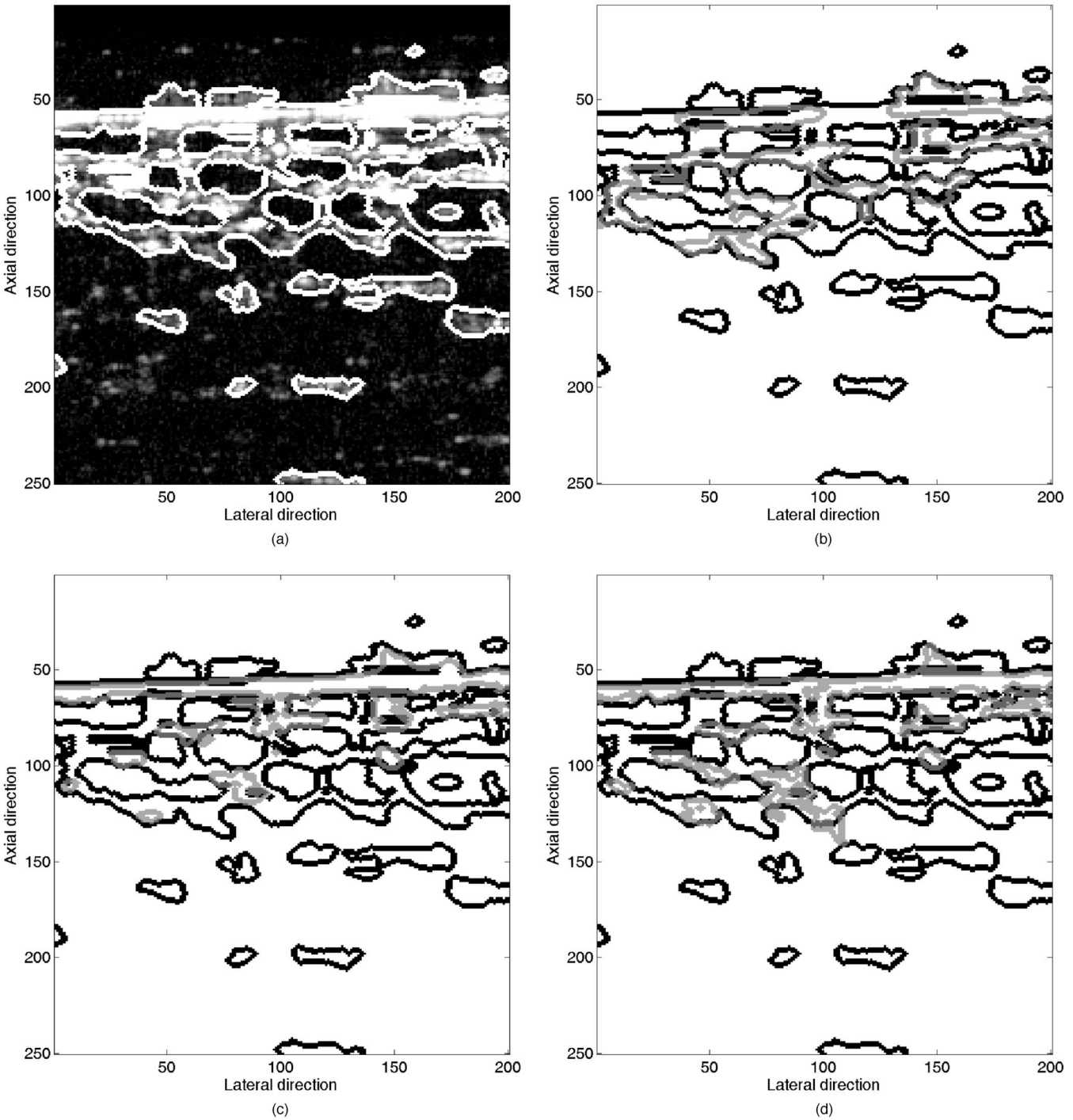

Fig. 13 Scenario onion: Comparison of three region growing approaches for segmentation of cell walls of onion tissue structure: (a) OCT B-scan showing cell structures of an onion and manual segmentation, (b) ARG, (c) PM-FRG, and (d) CD-FRG. For each evaluated method, the segmentation map shows the reference (manual segmentation) in black and the methods results in gray.

rat. The brain was dissected and scanned along a coronal section crossing the striatum, which contains white matter fibers.

3.5.2 *Segmentation of low scattering structures such as blood vessels*

Here, the seed detection and the region growing is performed on the inverted gray-scale image. Thus, dark areas of low scattering structures (e.g., vessel) are assigned a high intensity while areas of high scattering (e.g., tissue) are featuring low intensities. Thus, the seed detection and the region-growing algorithms can be applied as described.

Table 3 gives the details of all tested segmentation scenarios. For the evaluation of the segmentation performance for real images, a manual segmentation was performed by an OCT expert with 10 years of experience in OCT imaging. Visual results are presented in Figs. 11–16. Numerical results

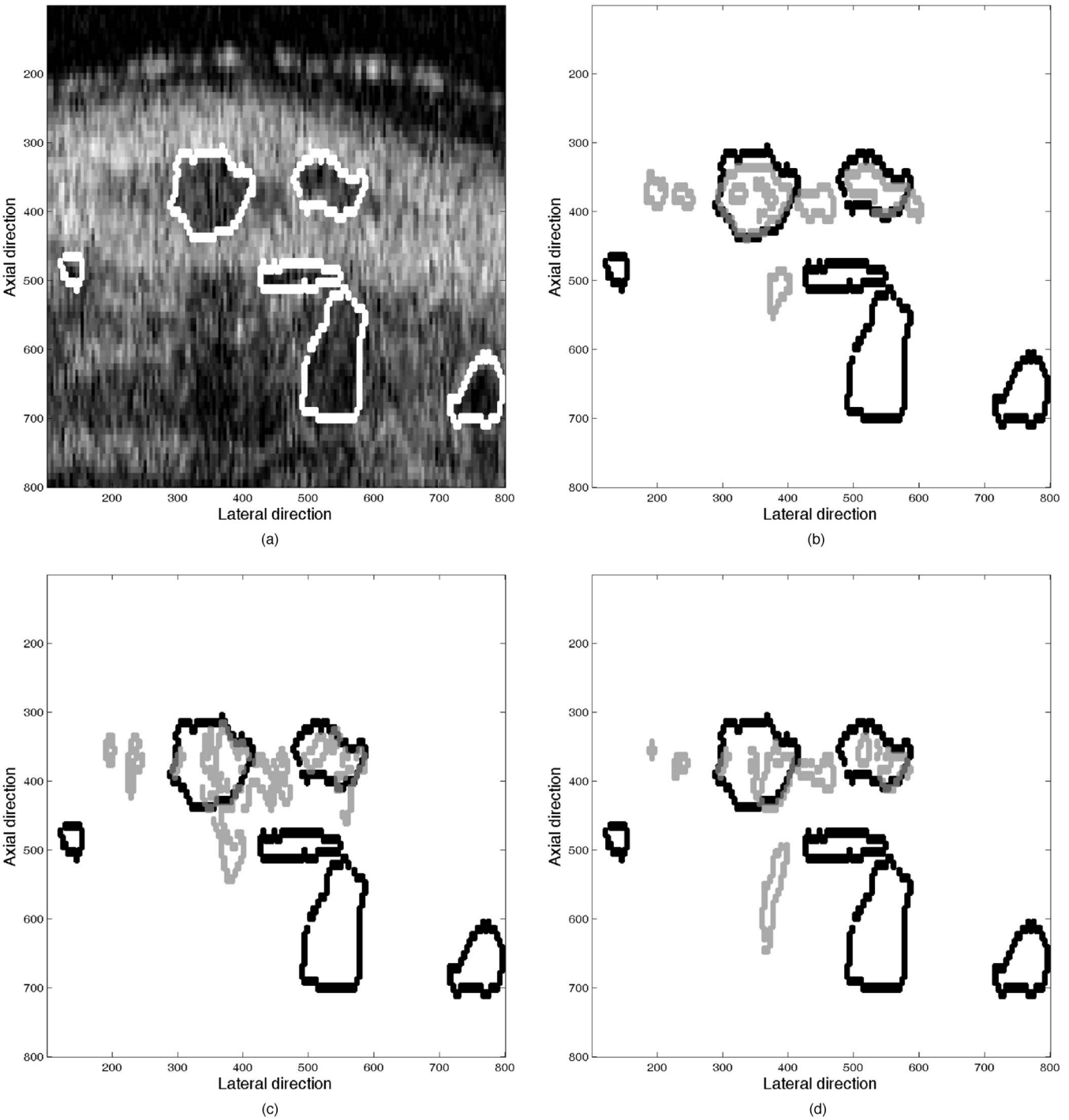

Fig. 14 Scenario urothel: Comparison of three region growing approaches for segmentation of vessels embedded into the urothel in an OCT image: (a) OCT B-scan showing the urothel with an embedded vessel and manual segmentation, (b) ARG, (c) PM-FRG, and (d) CD-FRG. For each evaluated method, the segmentation map shows the reference (manual segmentation) in black and the methods results in gray.

provide the JC index and HD with regard to the manual segmentation results and are listed in Tables 4 and 5.

4 Discussion

4.1 *Seed Detection*

Numerical results shown in Table 1 indicate that the method described in Sec. 2.2 provides a robust way to locate seed points for a subsequent region growing. Performance of the seed detection, however, is naturally dependent on the PCR. The higher the difference of the scattering properties of different structures is, the easier these structures can be discriminated. That is due to the stepwise approach of seed detection: the determination of the seed candidates is based on an analysis of the first derivative of the intensity course. A low PCR

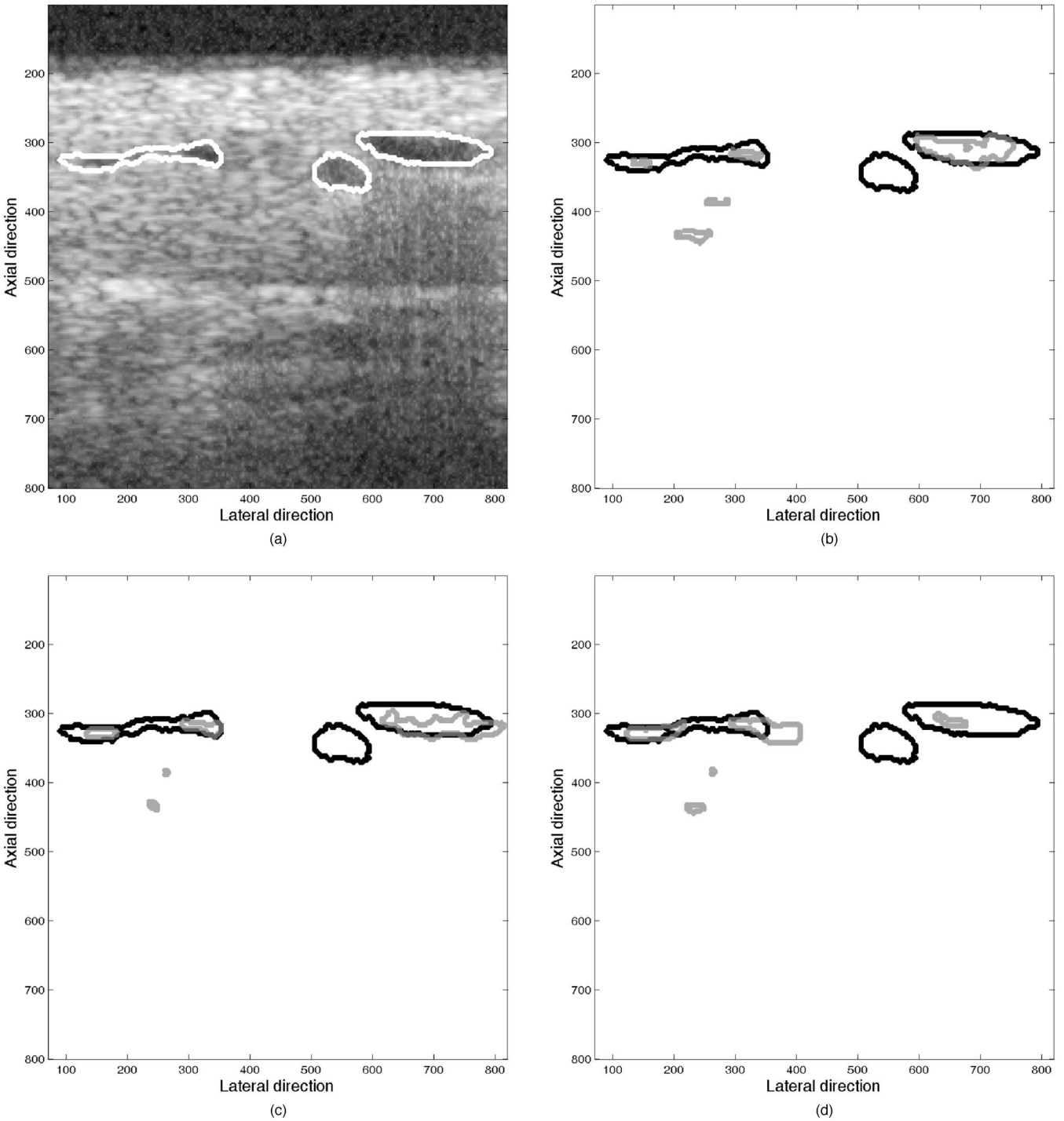

Fig. 15 Scenario intestine: Comparison of three region growing approaches for segmentation of vessels embedded into the intestine wall: (a) OCT B-scan showing vessels embedded into the intestine wall and manual segmentation, (b) ARG, (c) PM-FRG, and (d) CD-FRG. For each evaluated method, the segmentation map shows the reference (manual segmentation) in black and the methods results in gray.

will not lead to a significant change in the intensity, and peaks cannot be differentiated leading to a small set of peak candidates. Evaluation of extensive testing led to the heuristics based on ROC analysis for the choice of the threshold parameters depending on the PCR. Results show that for different PCR, the optimal parameters σ_1, σ_2, and σ_3 are almost constant and can thus be used for detection without previous determination of the PCR. This property enables the automatic nature of the process.

Also for the real OCT images, the presented results indicate an adequate performance of the seed detection. This especially applies to the task of detecting seeds in low scattering

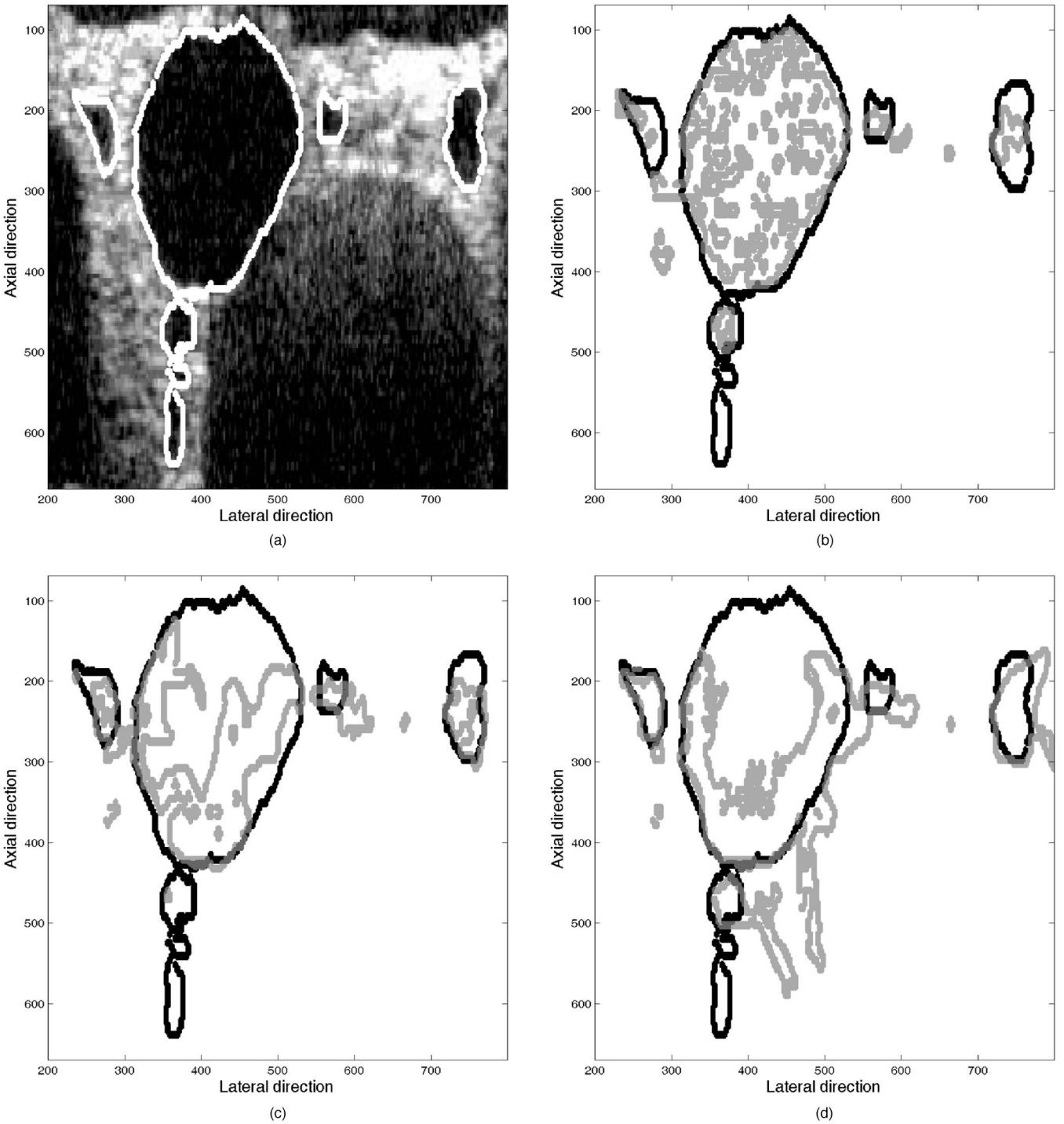

Fig. 16 Scenario egg: Comparison of three region growing approaches for segmentation of vessels embedded into the inner skin of an egg: (a) OCT B-scan showing vessels embedded into the inner skin of an egg and the results of the manual segmentation, (b) ARG, (c) PM-FRG, and (d) CD-FRG. For each evaluated method the segmentation map shows the reference (manual segmentation) in black and the method's results in gray.

structures, such as blood vessels, as the PCR of these structures in the inverted gray-scale images is relatively high. For the white matter identification in real OCT images, the PCR is found to be PCR $\approx 20 \ldots 25$. Transfering the results shown in Table 1, the seed detection would provide identification of over 90 percent of the structures in the real images.

4.2 *Region Growing*

Both, the ARG and FRG approaches are dependent on certain parameters, which have already been discussed in Sec. 3.4. Parameters for the simulation scenarios were chosen as specified in Sec. 3.4. In all test scenarios, the ARG and both of the

Table 4 Results of ARG, PM-FRG, and CD-FRG for segmentation of highly scattering tissue in comparison to expert manual segmentation.

	JC index			HD			Time (s)		
Scenario	ARG	PM-PRG	CD-FRG	ARG	PM-FRG	CD-FRG	ARG	PM-FRG	CD-FRG
wm1	0.3347	0.3232	0.3316	44.55	63.28	44.45	1.7	0.9	2.8
wm2	0.2371	0.077	0.1446	61.07	59.21	63.02	2.2	1.6	3.3
onion	0.3013	0.2564	0.2687	129.71	139.17	112.29	2.4	1.4	2.8

FRG have been applied with equal settings of the seed detection. Observing the simulation results in Table 2 and in Fig. 9, the following statements can be made: For all PCRs, the ARG approach provides a higher JC index while featuring a lower HD. This indicates less leakage while a better similarity between segmented and original regions is provided. This especially holds at a PCR of 20, which corresponds to the contrast ratio in real OCT images of brain matter.

It can be seen that for increasing PCR, the increase of the JC index of the PM-FRG is more substantial: The PM-FRG JC index increases by 46% for PCR increase from 20 to 30 while the ARG JC index increases only by 31% (see Fig. 9). This indicates that the higher the PCR is, the better the edge-sensitive filtering applies to the OCT images. Results of the ARG approach in Fig. 9 show that the adaptive homogeneity criterion applies well to the problem because the white matter structures are well segmented and only minor leakage can be observed. The results of the FRG in Fig. 10, however, show that substantial leakage occurs. This is indicates the major shortcoming of the FRG approaches in comparison to the ARG approach: the edge-sensitive filtering does alter the image. If the edge threshold parameter K is chosen too high then the edges will be blurred and the region growing will lead to leakage. This especially holds for the lower edges of the white matter structures because these feature a less distinct intensity difference to the neighboring regions than the higher edges. If the parameter K, however, is chosen too low, speckle-noise corruption will not be compensated and the subsequent region growing will lead to a lower JC index because no homogenous regions are provided after filtering.

Segmentation results performed on real images show the capability of the algorithms. Segmentation of different tissue types is demonstrated as two types of structures: one being bright and one being a dark region. Visual inspection indicates that the ARG approach is a better candidate for automated segmentation for the analyzed structures. Mainly ARG results show that white brain matter from real OCT B-scans and onion cell walls can be identified with a moderate presence of leakage (see Table 4 and Figs. 11–13). The numerical comparison to the manual segmentation of an OCT expert in Table 4 shows two tendencies: (*i*) For a comparable JC index (e.g., wm1), the HD of the ARG approach is smaller than for the results of the FRG approaches. (*ii*) If a comparable HD is achieved (e.g., wm2), the JC index of the ARG is higher than for the results of the FRG approaches. For the identification of low scattering structures, this tendency also holds (see Table 5). Visual inspection of the results also supports the conclusion that incorporation of OCT modeling into the segmentation approach provides a better structure identification. In the Egg scenario (see Fig. 16), ARG's segmentation results show an undesired oversegmentation, which is attributed to having the same homogeneity criterion parameters in all real images. This is a case in which the parameters should be tuned to provide a laxer region growing.

Interestingly, the time-consumption characteristics differ for both scenarios. While for identification of high scattering structures, the PM-FRG approach outperforms the ARG, the opposite behaviour can be observed for the identification of low scattering structures. In general, one would expect the FRG approach to be computationally more expensive than the ARG approach as an additional filtering step is required. Note, however, that time consumption also incorporates the process of region growing. A higher JC index at a comparable HD means that the region-growing process took longer as more structures of interest are segmented. Thus, time consumption does not directly allow a qualitative comparison of the approaches.

Table 5 Results of ARG, PM-FRG, and CD-FRG for segmentation of low scattering tissue in comparison to expert manual segmentation.

	JC index			HD			Time (s)		
Scenario	ARG	PM-PRG	CD-FRG	ARG	PM-FRG	CD-FRG	ARG	PM-FRG	CD-FRG
urothel	0.2101	0.1352	0.0974	54.64	59.07	59.07	0.3	0.7	0.26
intestine	0.3139	0.3018	0.1250	39.05	37.64	38.47	0.4	1.3	1.0
egg	0.6443	0.4330	0.3610	52.08	56.23	56.24	4.3	2.7	2.3

Considering the parameter sensitivity for both RGAs, heuristics can be drawn from extensive simulations (see Sec. 3.4). As stated in Sec. 3.4, results from simulated images indicate a preferable choice of parameters. For the ARG approach, this leads to a choice of $c_1=0.93\ldots0.97$, $c_2=1$, and $m'=4$. For the FRG approaches, a well-performing set of parameters is given by $N=40$, $K=4$, and $c_1=0.99$ and $c_2=1.01$.

Both seed detection and ARG are inherently dependent on the speckle size. While for the illustrated theoretical approach, the speckle size is assumed to equal 1 pixel in the image, this does not necessarily correspond to a real measurement scenario. There, the speckle size is related to the point-spread function of the measurement system. Therefore, speckle size might include more than 1 pixel. In that case, the outlined approach would have to be adapted, namely, by the extension of the pixel-related criteria based on an estimation of speckle size. For the seed detection, for instance, the ratio in Eq. (9) would compare the intensity at $\tilde{I}(z_k+n)$ with the intensity $\tilde{I}(z_k+n-s_z)$, where s_z would be the axial number of pixels occupied by a speckle. Equally important, the pixel neighborhood size would have to be adapted to the speckle size (the larger the speckle size, the larger the neighborhood).

The proposed region growing approach is presented for the identification of two distinct tissue structures. If tissue structures with more homogeneities are subject to segmentation (e.g., the retinal structure, which is a layered composite), the approach would have to be adapted. In this case, adaption would mostly affect the seed-detection intelligence, which would have to robustly identify at least one seed in each layer. As the growing criterion relies on a general OCT model, it should apply in its present form. Parameters, however, may have to be adapted to the respective task.

5 Conclusion

Summarizing this work, two approaches for the automated segmentation of tissue structures in OCT data have been developed. A two-step approach is taken: In a first step, automated seed detection for a subsequent region-growing algorithm is done. On the basis of the seeds, two alternatives for the homogeneity criterion within the region growing are proposed. The first region growing relies on an adaptive-neighborhood criterion and works on the original OCT data (ARG approach). The homogeneity criterion reflects the deterministic intensity course of OCT imaging in tissue and the speckle-noise corruption. The second approach uses an edge-sensitive filtered version of the image and applies a median-based homogeneity criterion (FRG approach).

Generally, the ARG approach provides a better segmentation for all contrast ratios of different tissue structures. Test results on white matter detection in brain imaging show the capabilities of the approaches. As a general tendency, results show that the ARG approach is more suitable for segmentation of structures in OCT images. Thus, it can be concluded that incorporation of an OCT model (deterministic intensity decay and speckle noise) does apply better to this image-processing task than filtering, which alters image information.

Further work to optimize the method's performance still remains, mainly to raise sensitivity in real scenarios and reduce leakage. However, the ARG approach shows strong potential to become a helpful tool in navigation and diagnosis. Other types of filtration for the FRG approach with a strict denoise-alteration compromise may also yield to better results. Because OCT has not yet been widely applied to neurosurgery, automated image processing opens the door to novel applications to be developed. The study in Ref. 3 shows evidence that the gray-white matter junction is a structure OCT can detect with high optical contrast and that it could serve as a landmark for guiding procedures such as deep brain stimulation. This application could benefit from the work presented in this paper. Segmentation of vessel structures, which was also shown to be feasible, could be used in other medical applications. Because the proposed algorithm is based on a general formulation of the OCT intensity model, it may be adapted for other segmentation tasks as well.

References

1. J. G. Fujimoto, "Biomedical imaging using optical coherence tomography," In *Quantum Electronics Conf. IOEC. Tech. Dig.* (1998).
2. B. E. Bouma and G. J. Tearney, *Handbook of Optical Coherence Tomography*, Marcel Dekker, New York (2002).
3. M. S. Jafri, S. Farhang, R. S. Tang, N. Desai, P. S. Fishman, R. G. Rohwer, C. Tang, and J. M. Schmitt, "Optical coherence tomography in the diagnosis and treatment of neurological disorders," *J. Biomed. Opt.* **10**(5), 051603 (2005).
4. D. L. Pham, C. Xu, and J. L. Prince, "Current methods in medical imaging," *Annu. Rev. Biomed. Eng.* **2**, 315–337 (2000).
5. R. M. Haralick, "Image segmentation techniques," in *Comput. Vis. Graph. Image Process.* Vol. **29**, pp. 100–132 (1985).
6. D. C. Ferandez, H. M. Salinas, and C. A. Puliafito, "Automated detection of retinal layer structures on optical coherence tomography images," *Opt. Express* **13**(25), 10200–10216 (2005).
7. H. Ishikawa, D. M. Stein, G. Wollstein, S. Beaton, J. G. Fujimoto, and J. S. Schuman, "Macular segmentation with optical coherence tomography," *Invest. Ophthalmol.* **46**, 2012–2017 (2005).
8. M. K. Garvin, M. D. Abramoff, R. Kardon, S. R. Russell, X. Wu, and M. Sonka, "Intraretinal layer segmentation of macular optical coherence tomography images using optimal 3-D graph search," *IEEE Trans. Med. Imaging* **27**(10), 1495–1505 (2008).
9. Y. Hori and Y. Yasuno, "Automatic characterization and segmentation of human skin using three-dimensional optical coherence tomography," *Opt. Express* **14**(5), 1862–1877 (2006).
10. J. Rogowska and M. Brezinski, "Image processing techniques for noise removal, enhancement and segmentation of cartilage oct images," *Phys. Med. Biol.* **47**, 641–655 (2002).
11. M. E. Brezinski, *Optical Coherence Tomography—Principles and Application*, Academic Press, New York (2006).
12. J. S. Lee, "Digital image enhancement and noise filtering by use of local statistics," *IEEE Trans. Pattern Anal. Mach. Intell.* **2**, 165–168 (1980).
13. V. S. Frost, J. A. Stiles, K. S. Shanmugan, and J. C. Holtzmann, "A model for radar images and its application to adaptive filtering of multiplicative noise," *IEEE Trans. Pattern Anal. Mach. Intell.* **4**, 157–165 (1982).
14. D. T. Kuan, A. A. Sawchuk, T. C. Strand, and P. Chavel, "Adaptive restoration of images with speckle," *IEEE Trans. Acoust., Speech, Signal Process.* **35**, 373–383 (1987).
15. P. Perona and J. Malik, "Scale-space and edge detection using anisotropic diffusion," *IEEE Trans. Pattern Anal. Mach. Intell.* **12**(7), 629–639 (1990).
16. J. Weickert, "Coherence-enhancing diffusion filtering," *Int. J. Comput. Vis.* **31**(2/3), 111–127 (1999).
17. G. Gilboa, N. Sochen, and Y. Y. Zeevi, "Image enhancement and denoising by complex diffusion processes," *IEEE Trans. Pattern Anal. Mach. Intell.* **25**(8), 1020–1036 (2004).
18. H. M. Salinas and D. C. Fernandez, "Comparison of pde-based nonlinear diffusion approaches for image enhancement and denoising in optical coherence tomography," *IEEE Trans. Med. Imaging* **26**(6), 761–771 (2007).
19. L. S. Dolin, "A theory of optical coherence tomography," *Radiophys. Quantum Electron.* **41**(10), 850–873 (1998).
20. P. E. Andersen, L. Thrane, H. T. Yura, A. Tycho, T. M. Jorgensen,

and M. H. Frosz, "Advanced modelling of optical coherence tomography systems," *Phys. Med. Biol.* **49**, 1307–1327 (2004).
21. I. Turchin, E. Sergeeva, L. Dolin, V. Kamensky, and N. Shakhova, "Novel algorithm of processing optical coherence tomography images for differentiation of biological tissue pathologies," *J. Biomed. Opt.* **10**(6), 064024 (2005).
22. J. M. Schmitt, A. Knuttel, M. Yadlowsky, and M. A. Eckhaus, "Optical-coherence tomography of a dense tissue: statistics of attenuation and backscattering," *Phys. Med. Biol.* **39**, 1705–1720 (1994).
23. S. W. Jeon, M. A. Shure, K. B. Baker, A. Chahlavi, N. Hatoum, and M. Turbay, "Optical coherence tomography and optical coherence domain reflectometry for deep brain stimulation probe guidance," *Proc. SPIE* **5686**, 487–494 (2005).
24. M. Ciuc, P. Bolon, E. Trouve, V. Buzuloui, and J.-P. Rudant, "Adaptive-neighborhood speckle removal in multitemporal synthetic aperture radar images," *Appl. Opt.* **40**(32), 5954–5966 (2001).
25. J. Liu, "Robust image segmentation using local median," in *Proc. of 3rd Canadian Conf. on Comput. and Robot Vis. (CRV'06)*, Quebec City, Canada, 7–9 June 2006, pp. 31, IEEE Computer Society, Washington, DC (2006).
26. W. P. Jones and G. W. Furnas, "Pictures of relevance: a geometric analysis of similarity measure," *J. Am. Soc. Inf. Sci.* **38**, 420–422 (1987).
27. V. Chalana and Y. Kim, "A methodology for evaluation of boundary detection algorithms on medical images," *IEEE Trans. Med. Imaging* **16**, 642–652 (1997).